PAPER

CrossMark
click for updates

Hollow Sr/Rh-codoped TiO₂ photocatalyst for efficient sunlight-driven organic compound degradation†

Chinh-Chien Nguyen,[a] Cao-Thang Dinh[b] and Trong-On Do*[a]

Sunlight-driven photocatalysis has emerged as a potential technology to address organic pollutant issues. Here, we report the first Rh-doped hollow-structured TiO₂ photocatalyst, which is highly active in the photocatalytic decomposition of organic pollutants under solar light. We achieved this by introducing Sr^{2+} as a co-doping agent, which stabilized the hollow structure at high temperatures and enabled us to control the oxidation state of Rh. The designed photocatalyst exhibited strong visible light absorption (up to 600 nm), and a very high surface area (up to 140 m^2 g^{-1}). As a result, the Sr/Rh-doped TiO₂ hollow photocatalysts demonstrated a photocatalytic efficiency (PE) of 0.242%, which was at least 8 times higher than that of commercial TiO₂ (0.03%) and 25 times higher than that of bulk Sr/Rh–TiO₂ (0.01%), in the photocatalytic decomposition of isopropanol under solar light irradiation.

Introduction

As a consequence of rapid global economic growth, environmental pollution by organic compounds has become one of the most critical issues for human society over the past four decades.[1] Photocatalytic decomposition of organic species in air and water offers an efficient solution to solve this problem through the utilization of solar energy and high performance photocatalysts.[2] Among the various photocatalysts developed to date, TiO₂-based photocatalysts continue to receive considerable attention because of their abundance, nontoxicity, and stability under photochemical conditions, which makes them highly suitable for scale-up in environmental remediation.[3]

Currently, most TiO₂ photocatalysts are based on the anatase phase, which is generally the most active phase of TiO₂.[4] Compared to the anatase phase, the rutile phase is often overlooked due to its relatively low specific surface area originating from its high temperature synthesis, and its poor light absorption. Nevertheless, it has been demonstrated that the rutile phase is a promising candidate for the degradation of organic pollutants because of its strong reduction potential and high O₂ adsorption capacity.[5,6]

One of the biggest limitations of TiO₂ is its large bandgap (>3 eV), which makes it active only in the UV region, which accounts for less than 5% of the solar spectrum. There have been numerous attempts to overcome the poor light absorption of TiO₂ under sunlight by methods including the sensitization of TiO₂ with dyes or small bandgap semiconductors, doping, and coupling TiO₂ with plasmonic nanostructures.[7] Among them, doping TiO₂ with Rh has emerged as a viable technique for the enhancement of visible light absorption.[8–12] Both Rh^{3+} and Rh^{4+} introduce sub-bands into the forbidden band of TiO₂. Rh^{3+} contributes a donor level to the valence band, thus reducing the band energy and shifting light absorption to the visible region, whereas Rh^{4+} introduces an electron acceptor level below the conduction band, which serves as a recombination site, reducing the activity of the materials, as shown in Fig. SI 1.†[6,13] Therefore, controlling the oxidation state of Rh in Rh-doped TiO₂ is critical to the photocatalytic enhancement of TiO₂.

Another approach to improve the performance of TiO₂ photocatalysts is through nanostructuring.[14] For example, photocatalysts based on hollow structures have attracted considerable attention because they improve the photoactivity of the catalyst by enhancing the separation of photogenerated charge carriers, shortening the charge diffusion length, and increasing the accessibility of active sites for reactants.[15] In addition, multiple reflections within the hollow cavity could improve the efficiency of light absorption, leading to the generation of additional electron–hole pairs.[16]

It is reasonable that combining the aforementioned approaches (*i.e.*, Rh doping and a hollow structure) would result in an efficient TiO₂-based photocatalyst with strong visible light absorption, good charge separation, and high surface active area. However, the design of such materials remains challenging because the introduction of Rh into the TiO₂ lattice requires high temperatures (>1000 °C), at which the hollow structure collapses because high surface energy induces

[a]Department of Chemical Engineering, Laval University, Quebec, G1V 0A8, Canada. E-mail: trong-on.do@gch.ulaval.ca; Fax: +1-418-656-5993; Tel: +1-418-656-3774

[b]Department of Electrical and Computer Engineering, University of Toronto, Toronto, ON, M5S 1A4, Canada

† Electronic supplementary information (ESI) available. See DOI: 10.1039/c6ra25987a

sintering effects. Therefore, using a stabilizer to maintain the surface area is critical and so far has not been explored in the development of high performance photocatalysts.

Here, we report the first Rh-doped hollow-structured TiO$_2$ photocatalyst, which is highly active in the photocatalytic decomposition of organic pollutants under sunlight. We achieved this by introducing simultaneous rhodium and strontium. We found that Sr^{2+} is as a codoping agent which stabilized the hollow structure at high temperatures, and contribute to control the chemical state of Rh in doped material.[16–18] The designed photocatalyst exhibited strong visible light absorption (up to 600 nm), and a very high surface area (up to 140 m^2 g^{-1}). As a result, the photoactivity of the photocatalyst was at least 8 times higher than those of commercial TiO$_2$ and bulk Sr/Rh–TiO$_2$ powders in the decomposition of isopropanol under solar radiation.
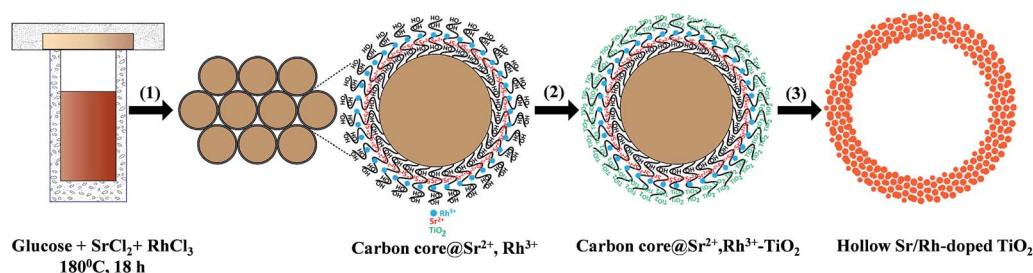
Results and discussion

Traditional methods for the synthesis of Rh-doped TiO$_2$ photocatalysts mainly focus on improving the doping of Rh in the TiO$_2$ lattice to enhance the visible light response of TiO$_2$. However, high-temperature calcination requirements for the substitution of Rh for Ti^{4+} in the TiO$_2$ matrix results in a photocatalyst with a very low surface area, which increases the charge recombination and decreases the number of active sites. Also, Rh^{3+}, which serves a critical role in the photocatalytic activity of Rh-doped TiO$_2$ under visible light irradiation, cannot

be obtained by conventional methods. Therefore, Rh^{3+}-doped TiO$_2$ materials with high surface areas are highly desired. Compared to traditional bulk Rh-doped TiO$_2$ photocatalysts, Sr/Rh-codoped TiO$_2$ offer several advantages. First, they exhibit a high surface area, owing to the presence of nanoparticles on the hollow wall. Therefore, the reaction can proceed inside and outside of the hollow spheres. Second, the co-incorporation of Sr cations enabled us to control the oxidation state of Rh, which leads to a significant enhancement in the visible light absorption and charge separation. Third, the homogeneous distribution of dopants significantly lowers the doping temperature as compared to conventional synthetic routes.

Hollow Sr/Rh–TiO$_2$ was prepared *via* a multistep pathway (Scheme 1) comprised of the following steps: (i) the one-pot synthesis of carbon colloidal spheres@Sr,Rh (C@Sr,Rh); (ii) coating C@Sr,Rh with TiO$_2$ by controlling the hydrolysis of tetraethyl titanium butoxide to obtain core–shell carbon sphere@Sr,Rh–TiO$_2$ microspheres (C@Sr,Rh–TiO$_2$); (iii) two-step calcination at 550 °C for 5 h to obtain anatase Sr/Rh–TiO$_2$-500, followed by calcination at 900 °C for 10 h to form rutile Sr/Rh–TiO$_2$-900. The calcination steps are critical for the substitution of Sr/Rh ions for Ti^{4+} in the TiO$_2$ crystal lattice and for the formation of the hollow structure with high porosity.

Fig. 1 shows the scanning electron microscopy (SEM) images of C@Sr,Rh–TiO$_2$, hollow Sr/Rh–TiO$_2$-550, and hollow Sr/Rh–TiO$_2$-900. The size of the C@Sr,Rh–TiO$_2$ microspheres was in the range of 500 nm to 2 μm prior to the two-step calcination (Fig. 1A). After calcination at 550 °C, the hollow structure was

Glucose + SrCl$_2$+ RhCl$_3$
180^{0}C, 18 h

Carbon core@Sr^{2+}, Rh^{3+}

Carbon core@Sr^{2+},Rh^{3+}-TiO$_2$

Hollow Sr/Rh-doped TiO$_2$

Scheme 1 Schematic illustration of the synthesis of hollow Sr/Rh-doped TiO$_2$ nanospheres: (1) one-pot synthesis of carbon colloidal spheres@Sr^{2+},Rh^{3+}, (2) loading of TiO$_2$ from the titanium alkoxide precursor, and (3) calcination at 550 °C for 5 h followed by calcination at 900 °C for 10 h.
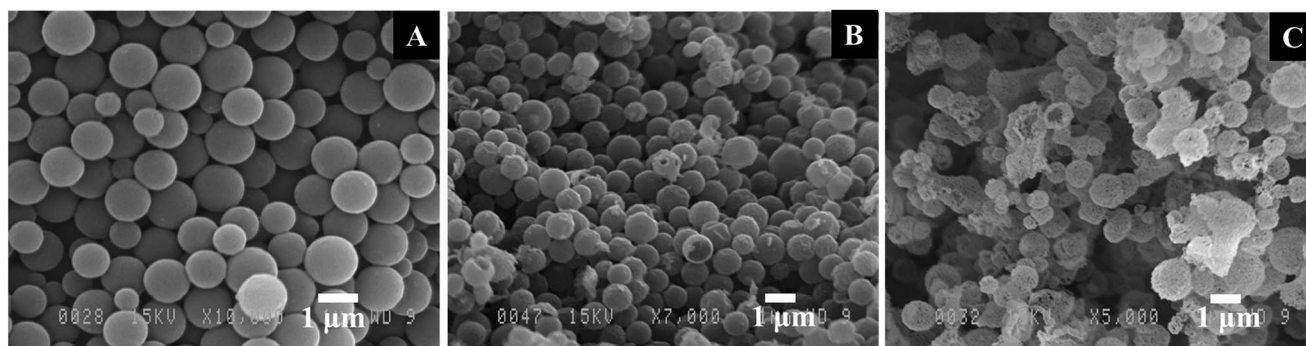

Fig. 1 SEM images of (A) carbon colloidal spheres@Sr,Rh@TiO$_2$ and hollow Sr/Rh–TiO$_2$ after calcination at (B) 550 °C and (C) 900 °C.
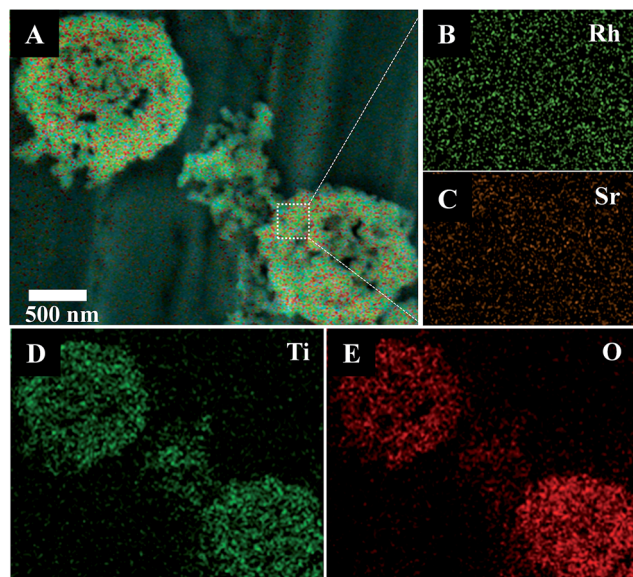
Fig. 2 EDX elemental mapping of hollow Sr/Rh–TiO$_2$-900: (A) SEM image; (B) Rh and (C) Sr at high magnification; (D) Ti; (E) O.

formed due to the combustion of the carbon colloidal spheres. Broken spheres were observed (Fig. 1B), confirming the formation of the hollow structure. The morphology and size of the hollow structures remained unchanged (500 nm to 2 μm) after calcination at 900 °C, as depicted in Fig. 1C. Fig. SI 2† shows a transmission electron microscopy (TEM) image of hollow Sr/Rh-doped TiO$_2$ after calcination at 900 °C, indicating the formation of particles (100–200 nm in size) on the wall of the hollow structure. Interestingly, we found that the incorporation of Sr^{2+} increased the stability of the hollow structure at high temperatures. As shown in Fig. SI 3 and SI 4,† the samples prepared using the same procedure in the absence of Sr^{2+} (Rh–TiO$_2$-900 and TiO$_2$-900) exhibited completely destroyed structures. In contrast, hollow TiO$_2$ structures were retained at high temperatures in the presence of Sr^{2+} with Rh^{3+} (Fig. 1C) or without Rh^{3+} (Fig. SI 5†). In general, the sintering-induced phase transformation of TiO$_2$ from anatase to rutile during calcination at high temperatures is responsible for the change of morphology and the collapse of hollow structure.[19,20] The addition of Sr^{2+} could lower the surface energy change during the TiO$_2$ phase transformation at high calcination temperatures thus preventing the sintering effect, and as a consequence, maintaining the hollow structure in the resulting hollow Sr/Rh–TiO$_2$-900.

Elemental mapping by energy-dispersive X-ray microscopy (EDX) from SEM analysis of a single hollow Sr/Rh–TiO$_2$-900 sphere clearly confirmed the homogeneous distribution of Ti, O, Rh, and Sr, as depicted in Fig. 2. The homogeneous distribution of these elements indicates efficient doping of Sr and Rh into the TiO$_2$ lattice without a phase separation. In this approach, using carbon colloidal spheres with a high density of OH groups on the surface facilitated the adsorption of Sr^{2+} and Rh^{3+} cations, which resulted in a homogeneous distribution of doping elements in the final hollow sphere products. The

chemical composition of the hollow Sr/Rh–TiO$_2$-900 was further analyzed by inductively coupled plasma mass spectrometry (ICP-MS); Rh and Sr contents of 2.0 and 2.3%, respectively, confirmed the successful synthesis of the hollow Rh/Sr-doped TiO$_2$ structure.

The X-ray diffraction (XRD) pattern of hollow Sr/Rh–TiO$_2$-900 (line a) and rutile TiO$_2$ (line b) (Fig. 3A) indicate the presence of rutile TiO$_2$ in the prepared photocatalysts, as neither SrTiO$_3$ nor Rh were detected.[21,22] The XRD peaks of hollow Sr/Rh–TiO$_2$-900 were slightly shifted to lower angles as compared to non-doped rutile-TiO$_2$, which could be due to the substitution of Rh^{3+} for Ti^{4+},[11] as Rh^{3+} ions (0.805 Å) are larger than Ti^{4+} ions (0.745 Å).[23] Because of the higher ionic radius of Sr^{2+} (1.12 Å) as compared to Ti^{4+} (0.61 Å), Sr^{2+} was unable to enter the TiO$_2$ lattice. Hence, Sr^{2+} could be present on the TiO$_2$ surface as Sr–O clusters.[24,25]

Fig. 3B shows the ultraviolet-visible (UV-vis) spectra of hollow Sr/Rh–TiO$_2$-550, hollow Sr/Rh–TiO$_2$-900, and bulk Rh–TiO$_2$-900. A remarkable enhancement in the light absorption along with a color alteration from white to yellow, as shown in Fig. SI 6,† was observed for hollow Sr/Rh–TiO$_2$-900 and Rh–TiO$_2$-900 compared to hollow Sr/Rh–TiO$_2$-550, indicating the effect of calcination temperature on the light absorption properties of Rh-doped TiO$_2$ materials. Higher calcination temperatures may favor the introduction of Rh to TiO$_2$ crystallites forming Rh-doped TiO$_2$ with a smaller bandgap. The UV-vis spectrum of Rh–TiO$_2$-900 revealed a discontinuous level at ~420 nm, which could be attributed to electron excitation from the donor levels formed by Rh^{3+} to the conduction band of rutile TiO$_2$.[11,26] In addition, a significant absorption band around 580–750 nm appeared in the UV-vis spectrum of this sample, indicating the presence of an acceptor level formed by Rh^{4+} in the TiO$_2$ structure. Thus, both Rh^{3+} and Rh^{4+} were present in the bulk Rh–TiO$_2$-900 sample. Compared to bulk Rh–TiO$_2$-900, hollow Sr/Rh–TiO$_2$-900 (in the presence of Sr) exhibited a simple absorption profile with an onset at ~420 nm, and the disappearance of the absorption band at around 580–750 nm. This suggested that only Rh^{3+} was present in hollow Sr/Rh–TiO$_2$-900.[26–28] The presence of Rh^{3+} ions in the hollow Sr/Rh–TiO$_2$-900 further confirm the important role of Sr^{2+} in this synthesis, as it not only prevented sintering induced by high temperature
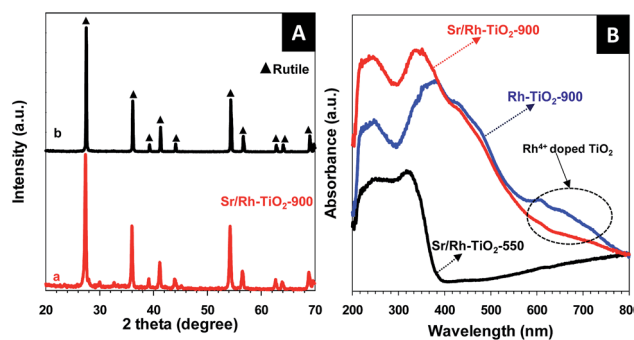

Fig. 3 (A) XRD pattern of the hollow Sr/Rh–TiO$_2$ sample after calcination at 900 °C and that of rutile TiO$_2$. (B) UV-vis spectra of the various hollow samples: Sr/Rh–TiO$_2$-550 (black line), Sr/Rh–TiO$_2$-900 (red line), and Rh–TiO$_2$-900 (blue line).

annealing, but also maintained the Rh^{3+} chemical state in the Rh-doped material. Fig. SI 7† shows the plot of $(\alpha h\nu)^2$ versus photon energy for the bandgap calculation of the samples. The band gap of hollow Sr/Rh–TiO$_2$-900 was calculated to be 2.25 eV, which was significantly lower than that of the hollow sample calcined at 550 °C (3.37 eV). The increased band gap of hollow Sr/Rh–TiO$_2$-550 as compared to anatase TiO$_2$ alone (3.2 eV) could be ascribed to the presence of Sr^{2+} on the TiO$_2$ surface, which reduced the particle size.[29]

To understand the surface composition and chemical states of the elements in the samples, X-ray photoelectron spectroscopy (XPS) was carried out for the hollow Sr,Rh-doped TiO$_2$-900 and Rh-doped TiO$_2$-900. The presence of Sr, Rh, Ti, and O in Sr/Rh–TiO$_2$-900 was confirmed by XPS, as depicted in Fig. 4A. As shown in Fig. SI 8,† for the Sr 3d XP spectrum, the deconvoluted peaks centered at 133.1 and 134.87 eV could be attributed to Sr 3d$_{5/2}$ and Sr 3d$_{3/2}$ of Sr–O-modified TiO$_2$ surface.[30] Fig. 4B shows the deconvoluted peaks of Rh 3d XPS spectra in hollow Sr/Rh–TiO$_2$-900 (a) and Rh–TiO$_2$-900 (b). It should be noted that isolated observation of Rh^{3+} and Rh^{4+} is ambiguous by XPS analysis. However, it is essential to consider the shifting of their binding energies because it would help to evaluate the electron density of Rh atoms contributing to confirm the chemical states in each sample. For the Rh–TiO$_2$-900, the Rh 3d XPS spectrum shows two peaks centered at 309.3 eV and 314.2 eV, which could be attributed to 3d$_{5/2}$ and 3d$_{3/2}$ of Rh^{3+} and Rh^{4+} chemical states, respectively.[31,32] Interestingly, these peaks were shifted −0.3 eV and appeared at 390.0 and 313.9 eV for the hollow Sr/Rh–TiO$_2$-900, which could be attributed to the higher electron density of Rh cations. In other words, the chemical states of Rh in the hollow Sr/Rh–TiO$_2$-900 is lower than that in Rh–TiO$_2$-900. This is associated with UV-vis analysis, which confirms mainly

presence of Rh^{3+} chemical state in the hollow Sr/Rh–TiO$_2$-900. Fig. 4C shows the Ti 2p XPS spectra of the hollow Sr/Rh–TiO$_2$-900 (line a) and Rh–TiO$_2$-900 (line b). The Rh–TiO$_2$-900 exhibited two peaks at binding energies of 458.2 and 464.1 eV, which could be assigned to Ti 2p$_{3/2}$ and Ti 2p$_{1/2}$ of Ti^{4+} in the rutile phase.[33] These peaks are −0.1 eV shifted compared to those of r-TiO$_2$, suggesting the replacement of Ti^{4+} by both Rh^{3+} and Rh^{4+}, which induced a higher electron density around Ti^{4+} atoms in the lattice, as depicted in Table SI-1.† In the case of hollow Sr/Rh–TiO$_2$-900, the Ti 2p$_{3/2}$ and Ti 2p$_{1/2}$ peaks appeared at the binding energies of 457.8 and 463.7 eV, respectively, which are −0.4 eV shifted compared to those of Rh–TiO$_2$-900. This indicates a significant increase in the electron density of Ti atoms in hollow Sr/Rh–TiO$_2$-900 compared to that in Rh–TiO$_2$-900 which further confirm the replacement of Ti^{4+} by Rh^{3+} in the hollow Sr/Rh–TiO$_2$-900. These results, in combination with the data obtained from UV-vis, suggest that Rh is presented in the hollow Sr/Rh–TiO$_2$-900 primarily in the form of Rh^{3+}. Fig. 4D presents the O 1s XP spectra of the hollow Sr/Rh–TiO$_2$-900 (line a) and Rh–TiO$_2$-900 (line b). Two peaks with binding energies of 529.3 and 530.1 eV were observed in the deconvoluted peaks of O 1s in Rh–TiO$_2$-900 (line b). The peak centered at 529.3 eV could be ascribed to the lattice oxygen in TiO$_2$, while other one at 530.1 eV could be attributed to strongly bound Ti–OH. Using the O 1s of rutile-TiO$_2$ alone as a reference (Table SI-1†), the O 1s peak (at 529.3 eV) of Rh–TiO$_2$-900 exhibited a negative shift in comparison to that of pristine rutile-TiO$_2$ (at 529.6 eV), which originated from the introduction of partially filled Rh^{4+} states within the band gap.[13] This may cause the downward shifting of Fermi level towards the valence band, which may decrease energy bands along with the reduction potential of photogenerated electrons and induce a negative impact on the photoactivity.[13,34,35] In contrast, a strong positive shift in O$_{1s}$ peak was observed (at 529.9 eV) for hollow Sr/Rh–TiO$_2$-900 in comparison to rutile-TiO$_2$ alone and Rh–TiO$_2$-900, for which the O$_{1s}$ peaks were centered at 529.9 and 530.5 eV. The increased binding energy of O$_{1s}$ in hollow Sr/Rh–TiO$_2$-900 could be assigned to the filling of Rh^{3+} states within the band gap, which caused the upward shifting of Fermi level towards the conduction band, which increase the energy bands along with the reduction potential of photogenerated electrons and has a positive impact on the photocatalytic activity.[36,37] These differences could explain the disadvantages of Rh^{4+} and the critical role of Rh^{3+} in doped photocatalysts. Therefore, the introduction of Sr^{2+} to Rh-doped TiO$_2$ favors the formation of Rh^{3+} in the doped TiO$_2$. In the absence of Sr^{2+}, Rh^{3+} oxidizes to Rh^{4+} to re-establish the charge balance, resulting in the formation of Rh^{4+}-doped TiO$_2$. In contrast, the presence of Sr^{2+} which could function as the critical factor limiting this oxidation process and leading to the formation of Rh^{3+}-doped TiO$_2$.

The photocatalytic activity of a catalyst is strongly dependent on the number of active sites on its surface. Thus, surface and porosity properties are the important parameters governing the performance of a photocatalyst because high specific surface area and large pore volume facilitate mass transfer and effectively promote the kinetics of the photocatalytic reaction. Therefore, the photocatalytic activity is significantly
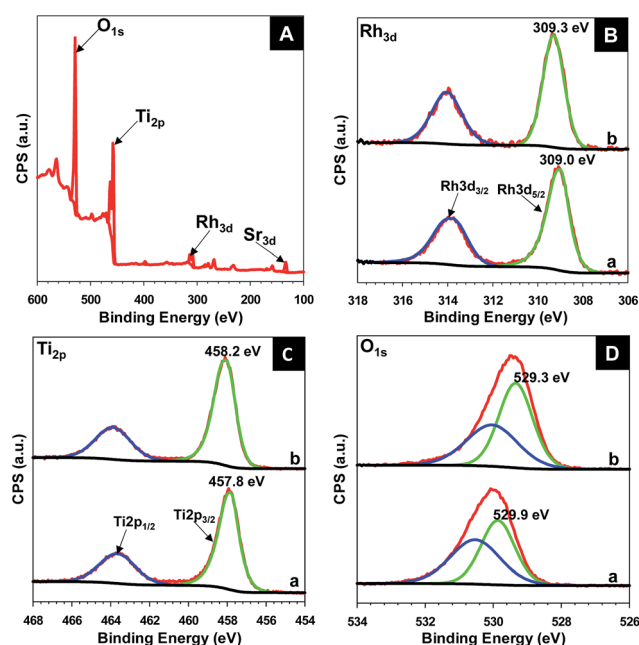

Fig. 4 XPS spectra of hollow Sr/Rh–TiO$_2$-900 (a) in comparison to those of Rh–TiO$_2$-900 (b) survey spectrum of hollow Sr/Rh–TiO$_2$-900 (A); XPS spectra of Rh 3d (B), Ti 2p (C), and O 1s (D).

Table 1 Physicochemical properties of various samples

Photocatalyst	TiO_2 phase	Morphology	% dopants (Rh^{3+}, Sr^{2+})	Band gap energy (eV)	Specific surface area $(m^2\ g^{-1})$
Hollow Sr/Rh–TiO_2-900	Rutile	Hollow spheres	2.0; 2.3	2.25	140
Hollow Sr/Rh–TiO_2-550	Anatase	Hollow spheres	2.0; 2.3	3.3	190
Sr/Rh–TiO_2-900-B	Rutile	Bulk crystals	2.0; 2.3	2.25	11
Rh–TiO_2-900	Rutile	Bulk crystals	2.1	2.0	3
r-TiO_2	Rutile	Bulk crystals	0; 0	3.1	10
TiO_2 (P25)	Anatase-rutile	Nanoparticles	0; 0	3.2	50

enhanced.[38,39] The specific surface areas of various samples were determined by N_2 physical adsorption measurements at 77 K. As shown in Fig. SI 9A,† hollow Sr/Rh–TiO_2-900 exhibits a high adsorption capacity in high relative pressure (P/P_0: from 0.8 to 1), suggesting a large porous structure.[40] The (Barrett–Joyner–Halenda) BJH pore size distribution obtained from the adsorption branch also reveals that the majority of pores are mainly from 2 to 10 nm, as depicted in Fig. SI 9B.† As shown in Table 1, the specific surface area of hollow Sr/Rh–TiO_2-900 reached 140 $m^2\ g^{-1}$, which was ~50 times higher than that of Rh–TiO_2-900 (3 $m^2\ g^{-1}$). Also, the specific surface area of hollow Sr/Rh–TiO_2-900 was significantly higher than those of r-TiO_2 (10 $m^2\ g^{-1}$) and commercial anatase TiO_2 (P25) (50 $m^2\ g^{-1}$), and ~13 times that of bulk Sr/Rh–TiO_2-900-B (Table 1). To the best of our knowledge, this hollow Sr/Rh–TiO_2-900 photocatalyst has one of the highest surface areas among doped rutile TiO_2 materials reported to date.[22,41,42] The above analyses afforded two important findings about the roles of Sr^{2+}: (i) the presence of Sr^{2+} functioned as a stabilizer to maintain the hollow structure leading to a high surface area photocatalyst; (ii) the chemical oxidation state of Rh^{3+} could be controlled in the doped TiO_2 with the co-presence of Sr^{2+}, which limited the oxidation of Rh^{3+} to Rh^{4+}. We believe that these two unique properties have a close relation in the resulted photocatalyst.

The photocatalytic activity of hollow Sr/Rh–TiO_2-900 was evaluated in the photodecomposition of isopropanol in water. So far, the isopropanol photodegradation is used as a model reaction for photo-oxidation of organic compounds.[43] Notably, Pt has been demonstrated to significantly improve the photocatalytic activity of TiO_2-based photocatalysts.[44] For free-Pt photocatalysts, only small amount of CO_2 was evolved from the decomposition of isopropanol for the hollow Sr/Rh–TiO_2-900 and no CO_2 was detected for the rest of samples, as shown in Fig. SI 10.† This indicates the critical role of Pt particles as co-catalyst. Therefore, the evolution of CO_2 from the decomposition of isopropanol under visible light ($\lambda \geq$ 420 nm) and solar light irradiation (see Experimental section) was monitored and compared with those observed using Sr/Rh–TiO_2-B, Rh–TiO_2-900 and r-TiO_2 with the optimized amounts of Pt loading, which were found to be ~1% Pt for the hollow Sr/Rh–TiO_2-900, ~0.3% for Sr/Rh–TiO_2-B and r-TiO_2 and ~0.1% for Rh–TiO_2-900, respectively. As shown in Fig. 5A, the photocatalytic activity of hollow Sr/Rh–TiO_2-900 was superior to those of Sr/Rh–TiO_2-B and Rh–TiO_2-900, as indicated by the higher CO_2 generation.
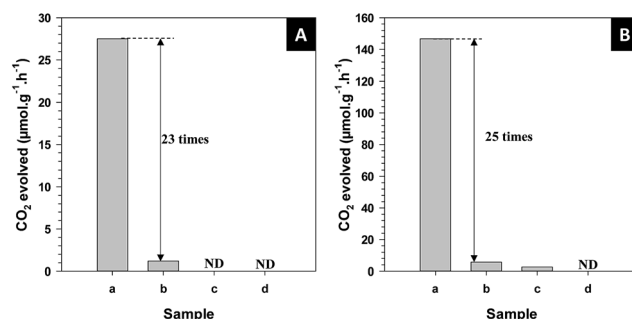

Fig. 5 CO_2 formation from the photodegradation of isopropanol of different types of photocatalysts with 1% Pt: (A) under visible light, (B) under solar simulator irradiation (AM 1.5 G, intensity 100 mW cm^{-2}): (a) hollow Sr/Rh–TiO_2-900; (b) bulk Sr/Rh–TiO_2-B; (c) rutile TiO_2; (d) Rh–TiO_2-900. ND: not detected.

The amount of CO_2 produced over the hollow Sr/Rh–TiO_2-900 under visible light was 27.5 μmol $g^{-1}\ h^{-1}$, which was more than 23 times higher than that of Sr/Rh–TiO_2-B (1.2 μmol $g^{-1}\ h^{-1}$). Under similar reaction conditions, CO_2 was not detected for the Rh–TiO_2-900 and r-TiO_2 samples, indicating their negligible photoactivities under visible light. As shown in Fig. 5B, hollow Sr/Rh–TiO_2-900 also exhibited a higher photoactivity than bulk Sr/Rh–TiO_2-B and r-TiO_2 under simulated solar irradiation. The amount of CO_2 evolved for hollow Sr/Rh–TiO_2-900 was 146 μmol $g^{-1}\ h^{-1}$, which was ~25 times higher than that of Sr/Rh–TiO_2-B (5.68 μmol $g^{-1}\ h^{-1}$), whereas r-TiO_2 and Rh–TiO_2-900 showed very low photoactivities. Compared to hollow Sr/Rh–TiO_2-550, hollow Sr/Rh–TiO_2-900 exhibited ~2.5 times higher CO_2 generation (Fig. SI 11†), despite the higher surface area of hollow Sr/Rh–TiO_2-550 (see Table 1). Moreover, the amount of CO_2 produced with the hollow Sr/Rh–TiO_2-900 catalyst was 6.6 times higher than that of commercial TiO_2 (P25). Therefore, the superior activity of hollow Sr/Rh–TiO_2-900 could be attributed to the synergistic effect of doping Rh^{3+} into the TiO_2 structure in the presence of Sr^{2+}, which causes strong solar light absorption, and a hollow structure with a high surface area. These features significantly enhanced the generation of electron–hole pairs and improved the charge separation during photocatalysis.

The photocatalytic efficiency (PE) for the photocatalytic decomposition of isopropanol under solar irradiation was calculated using the following equation:

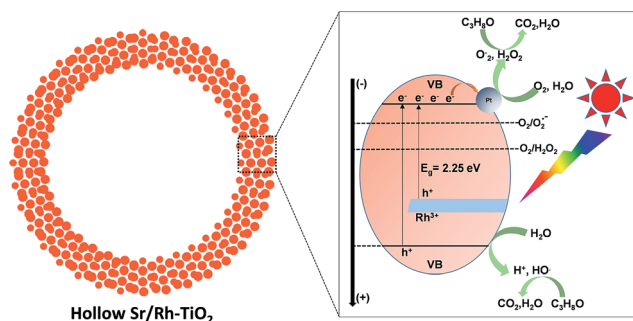$$PE = N_{\text{consumed photons for } CO_2}/N_{\text{incident photons}} \quad (1)$$

Fig. 6 Schematic illustration of the photodecomposition of organic isopropanol using hollow Sr/Rh−TiO$_2$-900 under solar light irradiation.

where $N_{\text{consumed photons for CO}_2}$ is the number of photons consumed for CO_2 generation and $N_{\text{incident photons}}$ is the total number of incident photons of simulated solar light. The details of this calculation were described previously.[45,46] The PE for CO_2 generation using hollow Sr/Rh−TiO$_2$-900 under simulated solar light was 0.242%, which is significantly higher than that using bulk Sr/Rh−TiO$_2$-900-B (∼0.01%) and TiO$_2$ (P25, 0.03%), confirming the promising application for solar-driven photodecomposition of organic pollutants.

The stability of the hollow Sr/Rh−TiO$_2$-900 was also studied by performing multi-recycling experiments under the same conditions, as shown in Fig. SI 12.† No significant change in the production of CO_2 was observed after 5 cycles. Also, the morphology was retained after the fifth cycle indicating the stability of the hollow Sr/Rh−TiO$_2$-900, as shown in Fig. SI 13.†

It has been demonstrated that rutile-TiO$_2$ contains a large amount of adsorbed oxygen on its surface.[47–51] Therefore, the photodecomposition of organic pollutants should be mainly directed toward the electron usage route, which produces strong oxidants ($O_2^{\bullet-}$, H_2O_2) ($E_{CB} = -0.7$ V $vs.$ standard hydrogen electrode (SHE); $O_2 + e = O_2^{\bullet-}$, -0.28 V $vs.$ SHE; $O_2 + 2H_2O + 2e^- = H_2O_2 + 2OH^-$, $+0.28$ $vs.$ SHE).[47–51] A mechanism for CO_2 generation with Sr/Rh-doped TiO$_2$ is proposed in Fig. 6. Hollow Sr/Rh−TiO$_2$-900 exhibited high photoactivity, which could be due to the synergistic contribution of efficient Rh^{3+} doping and high surface area. Indeed, efficient absorption of sunlight appeared to generate additional electron–hole pairs for the photodegradation of isopropanol into CO_2. Moreover, the high surface area of the hollow structure increases the number of exposed active sites for the photoreactions.[48] As a result, both as-photogenerated electron–hole pairs could contribute to produce strong oxidants inducing the efficient degradation of isopropanol.

Conclusions

We successfully prepared a novel type of hollow Sr/Rh-doped TiO$_2$ using carbon colloidal spheres as the sacrificial template. For the first time, we demonstrated that the introduction of Sr^{2+} to Rh-doped TiO$_2$ stabilizes the hollow structure and maintains the Rh^{3+} oxidation state of Rh in the doped material at high temperatures. The obtained photocatalyst exhibited high photoactivity in the degradation of isopropanol under visible light and simulated solar irradiation, owing to the synergistic

contributions of strong solar light absorption and high surface area. Therefore, our hollow material has significant potential for applications in water purification under natural solar illumination. Furthermore, this synthetic strategy can be extended to other hollow systems for a wide range of applications in catalysis and energy conversion. Work into gaining further insight into the mechanistic aspects of this process is in progress.

Experimental section

Chemicals

D-(+)-Glucose, hexachloroplatinic acid hexahydrate, strontium chloride, rhodium(III)nitrate, and tetraethyl titanium butoxide were purchased from Sigma-Aldrich. All reagents were used as received without further purification.

Material syntheses

Synthesis of carbon colloidal spheres@Sr/Rh(C@Sr/Rh). D-(+)-Glucose (17 g) was first dissolved in deionized water (160 mL). SrCl$_2$ (3.2 g) and an aqueous solution of Rh(NO$_3$)$_3$ (2 g, 1 mg mL^{-1}) were then added to the obtained solution. The resulting mixture was heated in a Teflon-lined autoclave at 180 °C for 18 h. Subsequently, the solid product was collected by centrifugation at 6000 ppm for 10 min, and was washed several times with water and ethanol before being dried overnight at 80 °C.

Synthesis of hollow Sr/Rh-doped TiO$_2$. The obtained carbon colloidal spheres C@Sr/Rh were loaded with a titanium alkoxide precursor as follows: C@Sr,Rh (2 g) was dispersed in anhydrous ethanol (30 mL) and then stirred for 1 h, followed by sonication for 15 min to ensure good dispersion. A solution of tetraethyl titanium butoxide in ethanol (15 mL, 50 mg mL^{-1}) was then added dropwise to the above solution with stirring for 1 h. Subsequently, a solution of water in ethanol (3.5 mg mL^{-1} water) was slowly added dropwise to the above solution to accelerate the hydrolysis of the titanium precursor. After stirring for 6 h, the resulting material was recovered by centrifugation, washed with anhydrous ethanol, and dried overnight at 80 °C in a vacuum oven to yield carbon colloidal spheres@Sr,Rh−TiO$_2$ (C@Sr/Rh−TiO$_2$). The as-prepared C@Sr/Rh−TiO$_2$ was loaded in an aluminum crucible and subjected to two-step calcination at different temperatures. The first step was carried out at 550 °C for 5 h (heating rate of 1 °C min^{-1}) to obtain anatase TiO$_2$ (denoted as hollow Rh/Sr−TiO$_2$-550). The second step was carried out at 900 °C for 10 h (heating rate of 3 °C min^{-1}) to achieve the rutile phase (denoted as hollow Sr/Rh−TiO$_2$-900).

Synthesis of Rh-doped TiO$_2$-900 and TiO$_2$-900. Rh-doped TiO$_2$-900 (denoted as Rh−TiO$_2$-900) and TiO$_2$-900 were synthesized using the same procedure as described above except that only Rh^{3+} was added to the mixture of colloidal spheres for the Rh−TiO$_2$-900 and neither Sr^{2+} or Rh^{3+} was used for undoped TiO$_2$-900 samples.

Synthesis of bulk Sr/Rh−TiO$_2$-900. Bulk Sr/Rh-doped TiO$_2$-900 (Sr/Rh−TiO$_2$-900-B) was prepared via a solid-state reaction for comparison. The starting materials (SrCl$_2$, Rh(NO$_3$)$_3$, and TiO$_2$) were mixed in the same atomic ratio as for hollow Sr/Rh−TiO$_2$-900. The mixture was calcined at 1000 °C for 10 h.

Characterization

Transmission electron microscopy (TEM) images of the samples were obtained using a JOEL JEM 1230 operated at 120 kV. Scanning electron microscopy (SEM) images were obtained using a JEOL 6360 operated at 15 kV. Powder X-ray diffraction (XRD) patterns of the samples were obtained using a Bruker SMART APEXII X-ray diffractometer equipped with a Cu Kα radiation source (λ = 1.5418 Å). X-ray photoelectron spectroscopy (XPS) measurements were carried out in the ion-pumped chamber (evacuated to 10^{-9} Torr) of a photoelectron spectrometer (Kratos Axis-Ultra) equipped with a focused X-ray source (Al Kα, $h\nu$ = 1486.6 eV). UV-vis spectra were recorded on a Cary 300 Bio UV-visible spectrophotometer. N_2 adsorption–desorption isotherms of the samples were obtained at 77 K using a Quantachrome Autosorb-1 MP analyzer. Prior to the measurements, the samples were outgassed under vacuum for 6 h at 150 °C.
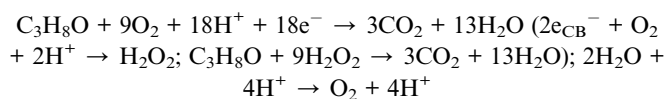
Photocatalytic tests

The photocatalytic decomposition of isopropanol was carried out in a top-irradiated reactor at ambient temperature and pressure. Prior to the photocatalytic tests, Pt was photodeposited on the catalyst. In a typical photocatalytic experiment, 20 mg of the photocatalyst, the optimum amount of photocatalyst for this photocatalytic reactor system, was dispersed in a 200 ppm solution of isopropanol in water. The reaction cell was then filled with fresh synthetic air (Prax air), stirred for 1 h to get steady-state regime prior to be illuminated with a solar simulator 150 W Xe lamp (AM 1.5 G, 100 mW cm^{-2}) for 3 h. To evaluate the photocatalytic activity of the samples under visible light, a UV cut-off filter ($\lambda \geq$ 420 nm) was used to produce visible light from the solar simulator. The amount of CO_2 gas generated during the reaction was analyzed using a gas chromatograph (Agilent 7820A) equipped with a thermal conductivity detector (TCD) and HP-PLOT U column, using helium as the carrier gas.

Photocatalytic efficiency (PE) calculations

Photocatalytic efficiency can be measured by the ratio of the number of product formed to the number of incident photons on the system and in a wavelength range λ_1–λ_2.[18,45,46] Under full solar irradiation, the number of incident photons calculated by integrating the intensity at each wavelength was 2.75×10^{17} photon per s per cm^2. A 4.5 cm^2 area of the sample was irradiated for 3 h. Therefore, the number of incident photons was calculated as follows:

$$N_{\text{incident photons}} = (2.75 \times 10^{17}) \times 3 \times 4.5 \times 3600$$
$$= 1.31 \times 10^{22} \text{ photons} \quad (2)$$

For CO_2 generation, assuming that the conversion of isopropanol (C_3H_8O) to CO_2 takes place on hollow Sr/Rh–TiO$_2$-900 according to the following equation, (six photons are required to produce one CO_2 molecule):

$$C_3H_8O + 9O_2 + 18H^+ + 18e^- \rightarrow 3CO_2 + 13H_2O \ (2e_{CB}^- + O_2 + 2H^+ \rightarrow H_2O_2; \ C_3H_8O + 9H_2O_2 \rightarrow 3CO_2 + 13H_2O); \ 2H_2O + 4H^+ \rightarrow O_2 + 4H^+$$

The amount of CO_2 generated under simulated solar light was determined to be 8.8 μmol. Therefore, the number of photons consumed to produce CO_2 under solar light illumination over 3 h was calculated as follows:

$$N_{\text{consumed photons for CO}_2} = 6 \times (8.8 \times 10^{-6}) \times (6.023 \times 10^{23})$$
$$= 3.18 \times 10^{19} \quad (3)$$

$$\text{PE} = N_{\text{consumed photons for CO}_2}/N_{\text{incident photons}}$$
$$= (3.18 \times 10^{19}/1.31 \times 10^{22}) \times 100 = 0.242\% \quad (4)$$

The same procedure was used to determine the PE of commercial TiO$_2$ (P25) and Sr/Rh–TiO$_2$-900-B.

Notes and references

1 L. G. Devi and R. Kavitha, *Appl. Catal., B*, 2013, **140**, 559–587.
2 X. Li, J. Yu and M. Jaroniec, *Chem. Soc. Rev.*, 2016, **45**, 2603–2636.
3 K. Nakata and A. Fujishima, *J. Photochem. Photobiol., C*, 2012, **13**, 169–189.
4 G. Odling and N. Robertson, *ChemSusChem*, 2015, **8**, 1838–1840.
5 S. Yurdakal, G. Palmisano, V. Loddo, V. Augugliaro and L. Palmisano, *J. Am. Chem. Soc.*, 2008, **130**, 1568–1569.
6 Q. Sun and Y. Xu, *J. Phys. Chem. C*, 2010, **114**, 18911–18918.
7 M. Nolan, A. Iwaszuk, A. K. Lucid, J. J. Carey and M. Fronzi, *Adv. Mater.*, 2016, **28**, 5425–5446.
8 L. R. Grabstanowicz, S. Gao, T. Li, R. M. Rickard, T. Rajh, D.-J. Liu and T. Xu, *Inorg. Chem.*, 2013, **52**, 3884–3890.
9 J. Tao, M. Yang, J. W. Chai, J. S. Pan, Y. P. Feng and S. J. Wang, *J. Phys. Chem. C*, 2014, **118**, 994–1000.
10 Y. Matsumoto, T. Shimuzu and E. Sato, *Electrochim. Acta*, 1982, **27**, 419–424.
11 R. Niishiro, R. Konta, H. Kato, W.-J. Chun, K. Asakura and A. Kudo, *J. Phys. Chem. C*, 2007, **111**, 17420–17426.
12 B. Liu, H. M. Chen, C. Liu, S. C. Andrews, C. Hahn and P. Yang, *J. Am. Chem. Soc.*, 2013, **135**, 9995–9998.
13 E. Glover, S. Ellington, G. Sankar and R. Palgrave, *J. Mater. Chem. A*, 2016, **4**, 6946–6954.
14 X. Chen and A. Selloni, *Chem. Rev.*, 2014, **114**, 9281–9282.
15 C. C. Nguyen, N. N. Vu and T.-O. Do, *J. Mater. Chem. A*, 2015, **3**, 18345–18359.
16 C.-T. Dinh, H. Yen, F. Kleitz and T.-O. Do, *Angew. Chem., Int. Ed.*, 2014, **53**, 6618–6623.
17 M.-H. Pham, C.-T. Dinh, G.-T. Vuong, N.-D. Ta and T.-O. Do, *Phys. Chem. Chem. Phys.*, 2014, **16**, 5937–5941.
18 C.-C. Nguyen, N.-N. Vu and T.-O. Do, *J. Mater. Chem. A*, 2016, 4413–4419.

19 J.-G. Yu, H.-G. Yu, B. Cheng, X.-J. Zhao, J. C. Yu and W.-K. Ho, *J. Phys. Chem. B*, 2003, **107**, 13871–13879.

20 Q. Mao, Y. Ren, K. H. Luo and S. Li, *J. Phys. Chem. C*, 2015, **119**, 28631–28639.

21 Y. Cao, X. Li, Z. Bian, A. Fuhr, D. Zhang and J. Zhu, *Appl. Catal., B*, 2016, **180**, 551–558.

22 L. Li, J. Yan, T. Wang, Z.-J. Zhao, J. Zhang, J. Gong and N. Guan, *Nat. Commun.*, 2015, **6**, 5881, DOI: 10.1038/ncomms6881.

23 R. T. Shannon, *Acta Crystallogr., Sect. A: Cryst. Phys., Diffr., Theor. Gen. Crystallogr.*, 1976, **32**, 751–767.

24 L. Escriche-Tur, J. Jover, M. Font-Bardia, G. Aullón and M. Corbella, *Inorg. Chem.*, 2015, **54**, 11596–11605.

25 Q. Wu, Q. Zheng and R. van de Krol, *J. Phys. Chem. C*, 2012, **116**, 7219–7226.

26 S. Kawasaki, K. Akagi, K. Nakatsuji, S. Yamamoto, I. Matsuda, Y. Harada, J. Yoshinobu, F. Komori, R. Takahashi and M. Lippmaa, *J. Phys. Chem. C*, 2012, **116**, 24445–24448.

27 R. Konta, T. Ishii, H. Kato and A. Kudo, *J. Phys. Chem. B*, 2004, **108**, 8992–8995.

28 Q. Wang, T. Hisatomi, S. S. K. Ma, Y. Li and K. Domen, *Chem. Mater.*, 2014, **26**, 4144–4150.

29 L. Kumaresan, M. Mahalakshmi, M. Palanichamy and V. Murugesan, *Ind. Eng. Chem. Res.*, 2010, **49**, 1480–1485.

30 S. Riedel, J. Neidhardt, S. Jansen, L. Wilde, J. Sundqvist, E. Erben, S. Teichert and A. Michaelis, *J. Appl. Phys.*, 2011, **109**, 094101.

31 C. Li, J. Liu, W. Gao, Y. Zhao and M. Wei, *Catal. Lett.*, 2013, **143**, 1247–1254.

32 S. Parres-Esclapez, I. Such-Basañez, M. J. Illán-Gómez, C. Salinas-Martínez de Lecea and A. Bueno-López, *J. Catal.*, 2010, **276**, 390–401.

33 W. Q. Fang, X. L. Wang, H. Zhang, Y. Jia, Z. Huo, Z. Li, H. Zhao, H. G. Yang and X. Yao, *J. Mater. Chem. A*, 2014, **2**, 3513–3520.

34 S. Bai, J. Jiang, Q. Zhang and Y. Xiong, *Chem. Soc. Rev.*, 2015, **44**, 2893–2939.

35 D. Lang, F. Cheng and Q. Xiang, *Catal. Sci. Technol.*, 2016, **6**, 6207–6216.

36 L. Li, P. A. Salvador and G. S. Rohrer, *Nanoscale*, 2014, **6**, 24–42.

37 J. Zhang, F. Ren, M. Deng and Y. Wang, *Phys. Chem. Chem. Phys.*, 2015, **17**, 10218–10226.

38 Q. Liang, Z. Li, Z. H. Huang, F. Kang and Q. H. Yang, *Adv. Funct. Mater.*, 2015, 6885–6892.

39 T. Weller, J. Sann and R. Marschall, *Adv. Energy Mater.*, 2016, **6**, 1600208.

40 J. Zhang, J. Yu, Y. Zhang, Q. Li and J. R. Gong, *Nano Lett.*, 2011, **11**, 4774–4779.

41 H. Hou, M. Shang, L. Wang, W. Li, B. Tang and W. Yang, *Sci. Rep.*, 2015, **5**, 15228.

42 R. Kaplan, B. Erjavec, G. Dražić, J. Grdadolnik and A. Pintar, *Appl. Catal., B*, 2016, **181**, 465–474.

43 Y. Li, S. Ouyang, H. Xu, X. Wang, Y. Bi, Y. Zhang and J. Ye, *J. Am. Chem. Soc.*, 2016, **138**, 13289–13297.

44 J. Yang, D. Wang, H. Han and C. Li, *Acc. Chem. Res.*, 2013, **46**, 1900–1909.

45 M. Liu, X. Qiu, M. Miyauchi and K. Hashimoto, *J. Am. Chem. Soc.*, 2013, **135**, 10064–10072.

46 S. E. Braslavsky, A. M. Braun, A. E. Cassano, A. V. Emeline, M. I. Litter, L. Palmisano, V. N. Parmon and N. Serpone, *Pure Appl. Chem.*, 2011, **83**, 931–1014.

47 D. O. Scanlon, C. W. Dunnill, J. Buckeridge, S. A. Shevlin, A. J. Logsdail, S. M. Woodley, C. R. A. Catlow, M. J. Powell, R. G. Palgrave and I. P. Parkin, *Nat. Mater.*, 2013, **12**, 798–801.

48 M. Buchalska, M. Kobielusz, A. Matuszek, M. Pacia, S. Wojtyła and W. Macyk, *ACS Catal.*, 2015, **5**, 7424–7431.

49 A. Fujishima, T. N. Rao and D. A. Tryk, *J. Photochem. Photobiol., C*, 2000, **1**, 1–21.

50 C. Chen, W. Ma and J. Zhao, *Chem. Soc. Rev.*, 2010, **39**, 4206–4219.

51 Y. Kakuma, A. Y. Nosaka and Y. Nosaka, *Phys. Chem. Chem. Phys.*, 2015, **17**, 18691–18698.